

Supporting Information

Materials and Methods

Preparation of lipid vesicles. The peptide-appended pillar[5]arene (PAP) channel shown in Fig. 1 was synthesized using protocols described previously (1). Lipids were purchased from Avanti Polar Lipids (Alabaster, AL) and used without further purification. For permeability measurements, liposomes were prepared by using the film rehydration method (2) while adding channels. PAP channels in DMSO (between 0 and 0.22 mg) were added to 6 mg of a 4:1 (mol/mol) phosphatidylcholine/ phosphatidylserine (PC/PS) mixture in CHCl_3 . The mixture was gently dried on a rotary evaporator under high vacuum to remove all solvent, and the resulting film was rehydrated with 1 mL buffer (10 mM Hepes, pH 7, 100 mM NaCl and 0.01% (w/v) NaN_3). For swelling experiments, the rehydration buffer was 10 mM Hepes, pH 7, 100 mM PEG600 and 0.01% (w/v) NaN_3 . After incubation on a stir plate at 4°C overnight, the suspension was extruded through 0.2 μm track-etched membranes (Whatman, UK) to obtain monodisperse, unilamellar vesicles. The size of the vesicles was determined by dynamic light scattering using a Zetasizer Nano instrument (Malvern Instruments Ltd., UK). To assess the dependence of the morphology of channel-lipid aggregates on the molar channel-to-lipid ratio (mCLR), channel-containing lipid membranes were formed using a slow dialysis method as described in a later section.

Water permeability measurements. The water permeability of pure and channel-containing lipid vesicles was measured at 10°C with an SF-300X stopped-flow instrument (KinTek Corp., PA). Vesicles were rapidly exposed to hypertonic/hypotonic solutions, causing them to shrink/swell due to the osmotic gradient. For shrinking experiments, the hypertonic osmolyte was 10 mM Hepes, pH 7, 300 mM NaCl, 0.01% (w/v) NaN_3 ; for swelling experiments, the hypotonic osmolyte was 10 mM Hepes, pH 7 and 0.01% (w/v) NaN_3 (lacking the 100 mM PEG600 in the buffer used to form the vesicles). The resulting changes in vesicle size were followed by recording light scattering at a wavelength of 600 nm and an angle of 90° (3). The light scattering signal was fit in the form of the sum of two exponential functions. The osmotic permeability (P_f) was calculated using the following formula (4):

$$P_f = \frac{k}{(S/V_0) \times V_w \times \Delta_{osm}} \quad (1)$$

where k is the exponential coefficient describing the change in light scattering (in shrinking experiments the coefficient with the smaller value (k_2) was used, while in swelling experiments the coefficient with the larger value (k_1) was used. See main text for details); S and V_0 are the initial surface area and volume of the vesicles, respectively; V_w is the molar volume of water, and Δ_{osm} is the osmolarity difference. When calculating the osmolarity difference in this equation, we have carefully considered the non-ideality of the solution. All the osmolarity difference values were experimentally measured on a freezing point osmometer (Model 3300, Advanced Instruments, Inc., MA), rather than approximating them with molarity concentration differences.

Water permeability of giant unilamellar vesicles (GUVs). GUVs with and without channels were prepared using a modified electroformation method, which was combined with hydrogel-based

microcontact printing (5). Briefly, small proteoliposomes prepared by using the film rehydration method were loaded onto patterned agarose gel stamps and then transferred onto an indium tin oxide (ITO) slide. The patterned ITO slide was partially dried and assembled into an electroformation chamber, a ‘sandwich’ flow chamber consisting of an upper ITO slide, intermediate PDMS spacer (with integrated inlet and outlet tubing), and the bottom ITO slide containing the patterned lipid/protein deposits. The chamber was filled with buffer containing 10 mM Hepes, pH 7, 100 mM PEG600, 0.01% (w/v) NaN₃ through inlet tubing with an alternating current electric field (2.1 V_{pp}, 50 Hz) applied for 2 hours. The resultant GUVs were detached from the ITO surface by decreasing the frequency from 50 Hz to 1 Hz for 10 min to assure the isolation of the vesicles’ interior from the outside. Replacing the buffer containing 100 mM PEG600 with buffer containing 100 mM glucose allowed the GUVs to settle on the slide for imaging by light microscopy. Hypotonic buffer, in which the glucose concentration was reduced to 80 mM, was injected into the chamber at a flow rate of 500 μ L/h using a syringe pump. The size change of GUVs upon exposure to hypertonic solution was followed for 1 hour by time-lapse imaging with an inverted Zeiss Axio Observer Z1 microscope equipped with an X-Cite Series 200 fluorescence lamp (EXFP Life Sciences, Ontario, Canada) and a CoolSNAP CCD camera (Photometrics, Tucson, AZ). The AxioVision 4.8.2 software (Carl Zeiss Microscopy, Oberkochen, Germany) was used for image acquisition.

Labeling procedure and estimating labeling efficiency. For labeling, 100 μ L PAP channel stock (5 mg/mL in DMSO) was mixed with 10 \times molar excess of both fluorescent dye (5-(and-6)-((N-(5-aminopentyl)amino)carbonyl)tetramethylrhodamine) (Invitrogen, CA) (9.18 μ L of 50 mg/mL in DMSO) and the cross-linker dicyclohexylcarbodiimide (DCC) (Thermo Fisher Scientific Inc., IL) (3.68 μ L of 50 mg/mL in DMSO). The reaction was performed in the dark at room temperature with stirring overnight. A Slide-A-Lyzer Mini Dialysis Unit with a 2 kDa MWCO with regenerated cellulose membrane (Thermo Fisher Scientific Inc., IL) was then used to remove residual free dye and DCC. The efficiency of dye removal was evaluated on a UV-Vis spectrophotometer (Nanodrop 2000c, Thermo Fisher Scientific Inc., IL) based on its specific absorbance wavelength at 544 nm and the Beer-Lambert law.

Dialysis was found to efficiently remove free dye while retaining nearly 100% of the PAP channel (Fig. S4). We also performed dialysis of pure dye solution. It was found that 92.6 \pm 2.2% of the free dye was removed after dialysis (Fig. S5, n=3). After cross-linking the dye to the channel and dialysis, 52.8 \pm 5.4% of the dye was retained (Fig. S6, n=3). Assuming ~7% of the free dye remained in solution after dialysis, approximately 40% of the dye was successfully cross-linked to PAP channels. Considering the 1:10 stoichiometry of PAP channel to dye used for the reaction, on average every channel was labeled with approximately 4 dye molecules.

Fluorescence correlation spectroscopy (FCS). The number of channels per vesicle was measured based on a fluorescence correlation spectroscopy (FCS) technique (6-8). Fluorescently labeled channels were incorporated into liposomes using the film rehydration method (2). The vesicles were dialyzed and subjected to size-exclusion chromatography to remove residual free dye. The fluorescence intensity $F(t)$ within a small confocal volume was monitored using a time-resolved single-photon counting module

(Becker-Hickl GmbH, Germany). The fluorescence fluctuation $\delta F(t)$, t (time) and τ (lag time) were used to calculate the autocorrelation function $G(\tau)$ (8):

$$G(\tau) = \frac{\langle \delta F(t) \delta F(t + \tau) \rangle}{\langle F(t) \rangle^2} \quad (2)$$

The specific expression of $G(\tau)$ is related to the geometry of the confocal volume (r and z are the radius and half height of the confocal volume, respectively), the characteristic diffusion time (τ_{Di}) of the fluorescent species i across a distance of r , and the average number (N) of fluorophores in the confocal volume. f_i is the fraction of fluorescent species i (8).

$$G(\tau) = \frac{1}{N} \sum_{i=1}^M f_i \left[\frac{1}{1 + \tau/\tau_{Di}} \right] \left[\frac{1}{1 + (r/z)^2 (\tau/\tau_{Di})} \right]^{1/2} \quad (3)$$

The number of the independent fluorescent molecules in the confocal volume is the inverse of $G(0)$. Thus, the number of labeled channels per vesicle can be calculated as the ratio of the number of particles in the confocal volume before and after detergent solubilization of the vesicles (6).

The labeling of PAP channels in our system was corroborated by the significantly different time frames of the autocorrelation functions of the three fluorescent species: free dye (~0.5 kDa), labeled channel in detergent micelles (~7.7 kDa, assuming that on average every channel was labeled with 4 dye molecules) and labeled channel incorporated into vesicles (Fig. 2F).

Molecular dynamics (MD) simulations. All MD simulations were performed using the molecular dynamics program NAMD (9). PAP channels, arranged in a regular array of 5×5 channels, were embedded in a 14.5×14.5 nm POPC bilayer (overlapping lipid molecules were deleted or moved to maintain the appropriate area per lipid). The electrically neutral system was solvated in TIP3P water using the autosolvate plugin of the visual molecular dynamics program, VMD (10). Existing CHARMM36 parameters (11) were used for water, non-bonded interactions, POPC, and phenylalanine arms, while the PAP backbone parameters were obtained from the paramchem website (12). Particle mesh Ewald full electrostatics were computed over a cubic grid with a ~1 Å spacing, and a smooth cutoff (8-10 Å) was implemented for van der Waals interactions. A 2-fs time step, rigid hydrogen bonds, and periodic boundary conditions were used. Unless stated otherwise, the temperature was held constant at 303 K using the Lowe-Andersen thermostat (13) with a rate of 50 ps⁻¹. The TIP3P water model (14) was used for each simulation. Atomic restraints, when used, were enforced using the constraints feature of NAMD with a spring constant of 1 kcal/mol·Å² for each restraint. Upon assembly, the energy of each system was minimized using the conjugate gradient method. Pressure constraints for NPT (constant number of particles N, constant pressure P, and constant temperature T) simulations (15) were enforced by the Langevin piston extendible along each axis with decay and a period of 800 fs, with the system length along the two membrane axes restrained to a 1:1 ratio. Effects of system drift were removed from the trajectory analysis by post-simulation realignment of the membrane.

To resolve steric conflicts and to allow the lipid bilayer to relax, minimization and equilibration was performed in NAMD while restraining the channel alpha carbons and fifteen selected carbons from the

central inner ring (dimethoxy benzene) of each channel. After a total of 64 ns of NVT (constant number of particles N, constant volume V, and constant temperature T) equilibration, the restraints were released and NPT simulation was performed for 160 ns. While the simulation was initiated with no water in the PAP channels, during the first 36 ns of equilibration water was observed to enter a few of the channels, connecting the two compartments separated by the membrane. Using the positions of the waters in the channels as a guide, a system was created from the end of the 36 ns MD trajectory in which waters were inserted into every channel. NPT simulations were then run of this system. The channel water positions were restrained for 9 ns to allow channel expansion, and the simulation was then continued for 125 ns with the restraints removed. On average, the root mean square deviation (RMSD) of the channel coordinates from their X-ray values reached 4.8 Å within 75 ns of unrestrained simulation, while the core dimethoxy benzene ring reached on average an RMSD of 0.4 Å within 5 ns (Fig. S10).

It has previously been shown that the osmotic permeability through a nano-channel can be determined by simulations under equilibrium conditions using the collective diffusion model (16). This model requires the definition of a volume of interest through which water permeates. We defined our channel volume of interest as a cylindrical region of 6 Å in diameter and 8 Å in height, aligned with the z axis (normal to the membrane plane) and positioned at the center of mass of the carbons of the dimethoxy benzene ring of the channel. The waters in this region were analyzed as described in the following paragraphs.

First, the vector displacement along the z axis of each water molecule in the region of interest was determined. To define the collective displacement coordinate, $n(t)$, the sum of the displacements was divided by the length of the volume along the pore axis to yield the one-dimensional displacement, which was integrated over the simulation time t for each channel in the trajectories. Then, the mean square displacement (MSD), $\langle n^2(t) \rangle$, was calculated to make use of the Einstein relation, where D is the diffusion coefficient:

$$\langle n^2(t) \rangle = 2Dt \quad (3)$$

The osmotic permeability P_f of each channel is proportional to D , where v_w is the volume of a water molecule:

$$P_f = v_w D \quad (4)$$

This relationship was used to determine the permeability P_f of each channel. The analysis was limited to MD trajectory data taken after 30 ns, identified in Fig. 3B as the point of convergence for the fraction of water-filled channels in the two systems. The permeability values were computed for each channel in each 18 ns segment of the MD trajectories. The average permeability and the standard deviation were obtained by averaging over all 18-ns segments of the trajectory and all channels present in the simulation system.

To test its appropriateness, the method was first used to calculate the permeability of AQP1 (16). The calculated value of $2.0(\pm 0.1) \times 10^{-13}$ cm³/s was within the range of previously determined values (1.4 to 2.9×10^{-13} cm³/s) (17). In our simulations, AQP1 was embedded in a POPE membrane, solvated, equilibrated in the NPT ensemble, then run in NVT for ~60 ns at 310 K. Other simulation parameters were similar to those used for the simulations of the PAP channels.

To build a model of densely packed PAP channels in a lipid bilayer (Fig. 4C), 20 copies of the PAP

channel were placed on a hexagonal grid and surrounded by POPC lipids. The parameters of the grid were the lattice parameters obtained by cryo-EM ($a=b=21$ Å and $\gamma=120^\circ$), whereas the coordinates of the channels were taken from a microscopic state observed after 120 ns equilibration of the assembled system initiated with water-filled channel, Fig. 3B. The channels were added to a POPC lipid bilayer preserving their unique equilibrated conformations. After solvation and a 12,000-step energy minimization that eliminated steric conflicts, the membrane was relaxed during a 1 ns equilibration in the NPT ensemble. By removing excess lipids and setting the rectangular periodic boundaries of the system to $x = 105$ Å, $y = 72.75$ Å, the system was reduced to a truly periodic hexagonal array. Another 12,000 steps of energy minimization removed the resulting steric conflicts. The system was then simulated for 4.6 ns in the NVT ensemble. Fig. 4C depicts the state of the system at the end of the simulation.

Self-assembly of PAP channel/lipid aggregates and EM imaging. PAP channel/lipid aggregates were produced by a slow dialysis procedure (18). First, 18 µg phosphatidylcholine and PAP channels (0 to 131 µg) were dissolved in chloroform and mixed at different mCLR. After evaporating the chloroform, the film was rehydrated with 60 µL dialysis buffer (10 mM HEPES, pH 7, 100 mM NaCl, 0.01% (w/v) NaN_3) initially containing 4% (w/v) OG. After incubation overnight, the PAP channel/lipid mixture was transferred into dialysis buttons (Hampton Research, CA) with a 2-kDa cut-off membrane, in which the final lipid concentration was 0.3 mg/mL. The detergent concentration (initially 4%, w/v) was gradually lowered by doubling the dialysis buffer volume with detergent-free buffer every 24 h until the OG concentration in the dialysis buffer reached 0.25% (w/v). The dialysis buffer was then replaced with detergent-free buffer three times every 8 h. The samples were harvested and adsorbed on glow-discharged carbon-coated EM grids (Ted Pella Inc., CA), stained with 0.75% uranyl formate, and imaged using a Techai G2 Spirit BioTwin transmission electron microscope (FEI).

Grids for cryo-EM analysis were prepared using the carbon sandwich technique using 4% (w/v) trehalose (19). Grids were transferred into a Polara electron microscope (FEI) operated at an acceleration voltage of 300 kV. Movies were recorded with a K2 Summit camera (Gatan) at a calibrated magnification of $40,607\times$ (nominal magnification of $31,000\times$) and a defocus ranging from -500 to -1400 nm. Stacks of 30 200-msec frames were collected at a dose rate of 8 e⁻/s/pixel, resulting in a total dose of 32 e⁻/Å². The image stacks were drift-corrected using the UCSF Image4 software (20), and the unit cell parameters were determined using the 2dx software (21).

Solute rejection. We noted that despite using the same osmolarity the apparent permeability induced by glucose was slightly lower than that induced by sucrose (Fig. S13). The disparity can be attributed to the imperfect rejection properties of the PAP channel for small solutes. In osmotically driven permeability tests, the osmotic gradient creates a driving force not only for water but also for small solutes to diffuse into the vesicles. If the channel is not completely impermeable to the small solutes, this decreases the osmotic gradient and thus offsets the volume change. The reflection coefficient (σ) can be used to estimate the relative rejection properties of a channel (22). Accordingly, we used solutes with different molecular weights as osmolyte, including glycine, arabinose, glucose, N-acetyl-D-glucosamine, sucrose and

Dextran500. The reflection coefficient is defined as $\sigma_{Solute} = J_{Solute} / J_{Dextran500}$, where σ_{Solute} is the reflection coefficient of the solute, J_{Solute} and $J_{Dextran500}$ are the measured water fluxes when solute and Dextran500 are used as osmolytes, respectively. The apparent permeability induced by small molecular weight osmolytes that can permeate the channel does not represent pure water conduction, and thus has to be corrected for by using its reflection coefficient ($P_f = P_{f(solute)} / \sigma_{Solute}$). This effect was taken into account when calculating the single-channel water permeability. The permeability induced by solutes with different molecular sizes under the same osmolarity conditions was different (Fig. S14). When the molecular weight of the osmolytes became larger, a significant increase in the exponential constant k_2 was observed. The permeability of vesicles formed at an mCLR of 0.005 increased from $0.00 \pm 0.03 \mu\text{m/s}$, when glycine was used as osmolyte, to $0.47 \pm 0.06 \mu\text{m/s}$, when Dextran500 was used as osmolyte. There was no increase in k_2 in control vesicles (Fig. S15). Thus, the apparent water permeability when glycine was used as an osmolyte was close to zero, indicating that the PAP channel is permeable to this small amino acid as previously reported (1).

Ion selectivity. The ion selectivity of the PAP channel was determined using a patch-clamp setup (Warner Instruments, LLC, CT). A 20 μL aliquot of diphytanoyl-phosphatidylcholine (diPhyPC) (10 mg/mL in chloroform) was dried using nitrogen gas. The film was dissolved in 5 μL n-decane and applied to a 200 μm aperture in the setup. After the re-dissolved lipid formed a thin film across the aperture, the *cis* chamber and the *trans* Delrin cup were filled with different salt solutions, with an Ag-AgCl electrode applied directly to the two solutions and the *cis* chamber being grounded. 1.0 μL lipid solution was then painted on the pretreated aperture to create a planar lipid bilayer with a capacitance of 80~120 pF. PAP channels were introduced into the lipid bilayer by injecting 3 μL of PAP channel (1 mM in DMSO) into the *cis* chamber followed by 5 min of mixing. The membrane current was measured with a Warner BC-535D bilayer clamp amplifier and recorded using PatchMaster (HEKA, Germany) with a sampling interval of 10 kHz. The signal was filtered with an 8-pole Bessel filter at 1 kHz (HEKA, Germany). The FitMaster software (HEKA, Germany) was used to analyze the data using a digital filter at 100 Hz. The reversal potential, obtained from the measured voltage-current data, was used to calculate the ion selectivity based on the Goldman-Hodgkin-Katz equation (23).

References

1. Chen L, *et al.* (2013) Chiral Selective Transmembrane Transport of Amino Acids through Artificial Channels. *J. Am. Chem. Soc.* 135(6):2152-2155.
2. Woodle MC & Papahadjopoulos D (1989) [9] Liposome preparation and size characterization. *Methods Enzymol.*, ed Sidney Fleischer BF (Academic Press), Vol Volume 171, pp 193-217.
3. Latimer P & Pyle BE (1972) Light Scattering at Various Angles: Theoretical Predictions of the Effects of Particle Volume Changes. *Biophys. J.* 12(7):764-773.
4. Borgnia MJ, Kozono D, Calamita G, Maloney PC, & Agre P (1999) Functional reconstitution and characterization of AqpZ, the E-coli water channel protein. *J. Mol. Biol.* 291(5):1169-1179.
5. Kang YJ, Wostein HS, & Majd S (2013) A Simple and Versatile Method for the Formation of Arrays of Giant Vesicles

- with Controlled Size and Composition. *Adv. Mater.* 25(47):6834-6838.
6. Erbakan M, *et al.* (2014) Molecular Cloning, Overexpression and Characterization of a Novel Water Channel Protein from *Rhodobacter sphaeroides*. *PLoS ONE* 9(1):e86830.
 7. Hoomann T, Jahnke N, Horner A, Keller S, & Pohl P (2013) Filter gate closure inhibits ion but not water transport through potassium channels. *Proc. Natl. Acad. Sci. U.S.A.* 110(26):10842-10847.
 8. Gullapalli RR, Mathura R, Dangaria JH, Butler PJ, & Tabouillot T (2007) Integrated multimodal microscopy, time-resolved fluorescence, and optical-trap rheometry: toward single molecule mechanobiology. *J. Biomed. Opt.* 12(1):014012.
 9. Phillips JC, *et al.* (2005) Scalable molecular dynamics with NAMD. *J. Comput. Chem.* 26(16):1781-1802.
 10. Humphrey W, Dalke A, & Schulten K (1996) VMD: Visual molecular dynamics. *J. Mol. Graphics* 14(1):33-38.
 11. Brooks BR, *et al.* (2009) CHARMM: The biomolecular simulation program. *J. Comput. Chem.* 30(10):1545-1614.
 12. Anonymous (<https://cgenff.paramchem.org/>).
 13. Koopman EA & Lowe CP (2006) Advantages of a Lowe-Andersen thermostat in molecular dynamics simulations. *J. Chem. Phys.* 124(20):204103.
 14. Jorgensen WL, Chandrasekhar J, Madura JD, Impey RW, & Klein ML (1983) Comparison of simple potential functions for simulating liquid water. *J. Chem. Phys.* 79(2):926-935.
 15. Martyna GJ, Tobias DJ, & Klein ML (1994) Constant pressure molecular dynamics algorithms. *J. Chem. Phys.* 101(5):4177-4189.
 16. Zhu F, Tajkhorshid E, & Schulten K (2004) Collective Diffusion Model for Water Permeation through Microscopic Channels. *Phys. Rev. Lett.* 93(22):224501.
 17. Zhu F, Tajkhorshid E, & Schulten K (2002) Pressure-Induced Water Transport in Membrane Channels Studied by Molecular Dynamics. *Biophys. J.* 83(1):154-160.
 18. Kumar M, Habel JEO, Shen Y-x, Meier WP, & Walz T (2012) High-Density Reconstitution of Functional Water Channels into Vesicular and Planar Block Copolymer Membranes. *J. Am. Chem. Soc.* 134(45):18631-18637.
 19. Gyobu N, *et al.* (2004) Improved specimen preparation for cryo-electron microscopy using a symmetric carbon sandwich technique. *J. Struct. Biol.* 146(3):325-333.
 20. Li X, *et al.* (2013) Electron counting and beam-induced motion correction enable near-atomic-resolution single-particle cryo-EM. *Nat Meth* 10(6):584-590.
 21. Gipson B, Zeng X, Zhang ZY, & Stahlberg H (2007) 2dx—User-friendly image processing for 2D crystals. *J. Struct. Biol.* 157(1):64-72.
 22. Meinild A-K, Klaerke DA, & Zeuthen T (1998) Bidirectional Water Fluxes and Specificity for Small Hydrophilic Molecules in Aquaporins 0–5. *J. Biol. Chem.* 273(49):32446-32451.
 23. Hille B (2001) *Ion Channels of Excitable Membranes* (Sinauer Associates, Incorporated) pp 341-347.
 24. Fei Z, *et al.* (2005) A Synthetic Zwitterionic Water Channel: Characterization in the Solid State by X-ray Crystallography and NMR Spectroscopy. *Angew. Chem. Int. Ed.* 44(35):5720-5725.
 25. Kaucher MS, *et al.* (2007) Selective Transport of Water Mediated by Porous Dendritic Dipeptides. *J. Am. Chem. Soc.* 129(38):11698-11699.
 26. Le Duc Y, *et al.* (2011) Imidazole-Quartet Water and Proton Dipolar Channels. *Angew. Chem. Int. Ed.* 50(48):11366-11372.

27. Hu X-B, Chen Z, Tang G, Hou J-L, & Li Z-T (2012) Single-Molecular Artificial Transmembrane Water Channels. *J. Am. Chem. Soc.* 134(20):8384-8387.
28. Zhou X, *et al.* (2012) Self-assembling subnanometer pores with unusual mass-transport properties. *Nat Commun* 3:949.
29. Walz T, *et al.* (1997) The three-dimensional structure of aquaporin-1. *Nature* 387(6633):624-627.
30. Hite RK, Li Z, & Walz T (2010) Principles of membrane protein interactions with annular lipids deduced from aquaporin-0 2D crystals. *The EMBO Journal* 29(10):1652-1658.
31. Holt JK, Noy A, Huser T, Eaglesham D, & Bakajin O (2004) Fabrication of a Carbon Nanotube-Embedded Silicon Nitride Membrane for Studies of Nanometer-Scale Mass Transport. *Nano Lett.* 4(11):2245-2250.
32. Ge L, *et al.* (2012) Vertically-aligned carbon nanotube membranes for hydrogen separation. *RSC Advances* 2(12):5329-5336.
33. Mohammad M, Khan MB, Sherazi TA, Anguita J, & Adikaari D (2013) Fabrication of Vertically Aligned CNT Composite for Membrane Applications Using Chemical Vapor Deposition through In Situ Polymerization. *J. Nanomater.* 2013:5.
34. Baek Y, *et al.* (2014) High performance and antifouling vertically aligned carbon nanotube membrane for water purification. *J. Membr. Sci.* 460:171-177.
35. Holt JK, *et al.* (2006) Fast Mass Transport Through Sub-2-Nanometer Carbon Nanotubes. *Science* 312(5776):1034-1037.
36. Zeidel ML, Ambudkar SV, Smith BL, & Agre P (1992) Reconstitution of functional water channels in liposomes containing purified red cell CHIP28 protein. *Biochemistry* 31(33):7436-7440.
37. Murata K, *et al.* (2000) Structural determinants of water permeation through aquaporin-1. *Nature* 407(6804):599-605.
38. Noy A, *et al.* (2007) Nanofluidics in carbon nanotubes. *Nano Today* 2(6):22-29.

Table S1. Comparison of literature permeability data on artificial water channels

Artificial water channel	Pore size (Å)	Water conduction measurements	Single-channel permeability	Morphology of self-assembled aggregates
Helical tube assembled by zwitterionic coordination polymers formed by reaction of <i>N,N'</i> -diacetic acid imidazolium bromide with zinc (24)	2.6	Not studied	The authors state that the water conduction rate should be much lower than that of AQPs because of the presence of hydrogen bonds between the encapsulated water molecules and the inner oxygen atoms of the channel.	Not studied
Helical pore assembled from dendritic dipeptides (25)	14.5	Studied by dynamic light scattering experiments (not stopped flow, and thus with much lower time resolution) on giant unilamellar vesicles	No permeability data reported, just visual observations indicating that the channel is capable of conducting water.	Vesicles assembled, only for functional studies
Tubular architectures assembled by imidazole compounds with urea ribbons ^a (26)	2.6	Studied by dynamic light scattering experiments (not stopped flow) on channels incorporated into vesicles and using hypotonic conditions	~20 water molecules/s	Vesicles assembled, only for functional studies
Hydrazide-appended pillar[5]arenes ^b (27)	6.5	Studied by dynamic light scattering experiments (not stopped flow) on channels incorporated into vesicles and using hypotonic conditions	~40 water molecules/s	Vesicles assembled, only for functional studies
Tubular channels assembled by hexa (<i>m</i> -phenylene ethynylene) macrocycles ^c (28)	6.4	Studied by fluorescence stopped-flow measurements on channels incorporated into vesicles; determined using hypertonic conditions	~4.9×10 ⁷ water molecules/s	Vesicles assembled for functional studies, and long tubular structures.
Peptide-appended pillar[5]arenes (this work)	~5	Studied by stopped flow-based light scattering experiments combined with channel counting by FCS on channels incorporated into vesicles and using both hypertonic and hypotonic conditions	~3.5×10 ⁸ water molecules/s in swelling mode ~3.7×10 ⁶ water molecules/s in shrinking mode	With increasing mCLRs, the PAP channel/lipid aggregates change from small vesicles, to larger vesicles, and finally to flat membranes (and in some cases 2D arrays).

Note:

^a For the imidazole compound (structure **2** in ref 26), the authors reported the water transport rate activity ($k=1.0\times 10^{-3} \text{ min}^{-1}=1.67\times 10^{-5} \text{ s}^{-1}$) when the liposomes were exposed to a ~0.2 M NaCl hypotonic solution. The diameter of the liposomes was 100 nm. Therefore, according to $P_f = k/((S/V_0)\times V_w\times \Delta_{\text{osm}})$, the osmotic water permeability (P_f) was $7.7\times 10^{-9} \text{ cm/s}$. Assuming that a channel consists of 12 imidazole compound molecules as shown in Fig. 4 of ref 26, the mCLR was 0.061 (100 μL of a 11 mM lipid stock vs. 20 μL of a 40 mM imidazole compound stock). The sum of outer and inner surface areas was $\pi/4\times d^2+\pi/4\times (d-5)^2=56,852 \text{ nm}^2$, assuming that the bilayer thickness was 5 nm. The average cross-sectional area of a lipid was 0.35 nm², and that of the imidazole tetrad is ~1 nm². The theoretical insertion

number of the channel was ~4,200 per vesicle, assuming that all imidazole compounds incorporated into the vesicle and self-assembled into channels. Therefore, the single-channel permeability was $\sim 5.8 \times 10^{-22}$ cm³/s and ~20 water molecules/s.

^b For the hydrazide-appended pillar[5]arenes (structure **3** in ref 27), the authors reported that the water permeability (P_f) was 8.6×10^{-10} cm/s. The mCLR was 0.003. The diameter of the vesicles was 150 nm. The sum of outer and inner surface areas was $\pi/4 \times d^2 + \pi/4 \times (d-5)^2 = 132,261$ nm², assuming that the bilayer thickness was 5 nm. The average cross-sectional area of the lipid was 0.35 nm², and that of the channel was 1.43 nm². The theoretical insertion number of the channel was ~560 per vesicle, assuming that all channel molecules incorporated into the vesicles. Therefore, the single-channel permeability was $\sim 1.1 \times 10^{-21}$ cm³/s and ~40 water molecules/s.

^c For the tubular channels based on hexa (*m*-phenylene ethynylene) macrocycles (structure **1a** in ref 28), the authors reported that the net water permeability (P_f) was 7×10^{-4} cm/s. The molar lipid-to-macrocycle monomer ratio was 50/1, with each channel requiring about 10 monomers. The mCLR was 0.002. The diameter of the vesicles was 100 nm. The sum of outer and inner surface areas was $\pi/4 \times d^2 + \pi/4 \times (d-5)^2 = 56,852$ nm², assuming that the bilayer thickness was 5 nm. The average cross-sectional area of the lipid was 0.35 nm², and that of the channel was estimated as $\pi/4 \times \text{column diameter}^2 = 8.24$ nm². The theoretical insertion number of the channel was ~155 per vesicle, assuming that all channel molecules incorporated into the vesicle. Therefore, the average single-channel permeability was $\sim 1.42 \times 10^{-15}$ cm³/s and $\sim 4.89 \times 10^7$ water molecules/s. This value is close to the value that was reported in this study when the pore open probability was taken into consideration.

Table S2. Size of octyl glucoside (OG) micelles (2%, w/v) containing lipid (6 mg/mL) or PAP channel (0.22 mg/mL) or both as determined by dynamic light scattering (data shown are average of triplicate experiments with error representing standard deviation).

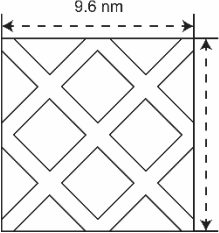
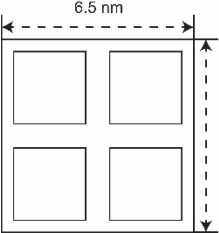
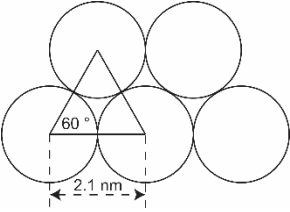
Sample	Diameter (nm)
OG micelles	7.8±0.2
Lipid+OG micelles	8.0±0.2
Channel+OG micelles	8.4±0.2
Channel+lipid+OG micelles	8.5±0.1

Table S3. Ion permeability ratio, P_X/P_{K^+} of the PAP channel

Ion	P_X/P_{K^+}
Cl ⁻	0.10
NH ₄ ⁺	3.77
Li ⁺	0.15
Na ⁺	0.25
Rb ⁺	2.02
Cs ⁺	2.22

Note: data are from the voltage-current relationship of the PAP channel shown in Fig. S17.

Table S4. Packing density of AQPs, CNTs and the PAP channel

	Unit cell dimension	Packing density ($\#/\mu\text{m}^2$)	Reference
Aquaporin-1		8.6×10^4	(29)
Aquaporin-0		9.5×10^4	(30)
CNTs		0.4×10^3	(31)
		0.1×10^3	(32)
		0.2×10^3	(33)
		0.7×10^3	(34)
		2.5×10^3	(35)
PAP channel		2.6×10^5	This study

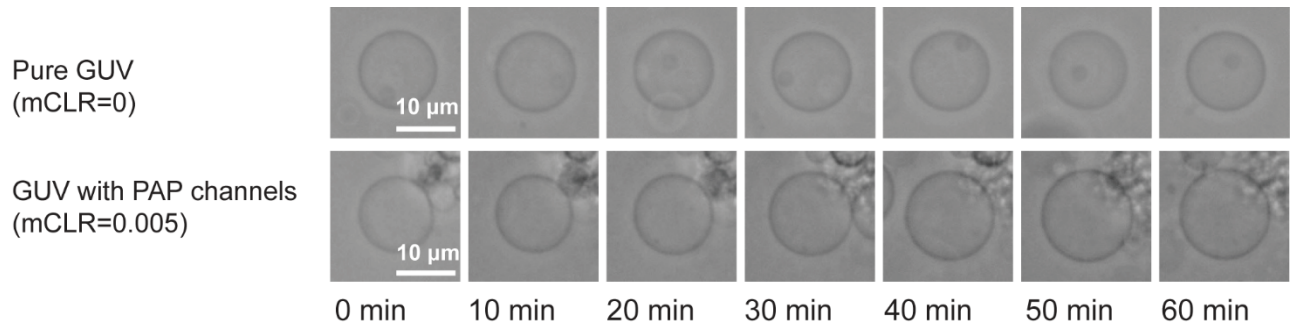


Fig. S1. Water permeability measurements using giant unilamellar vesicles (GUVs). Phase contrast images of GUVs formed at mCLRs of 0 and 0.005 for a period of one hour after exposure to 20 mM glucose hypotonic solution showing that the GUV containing PAP channels swells much faster.

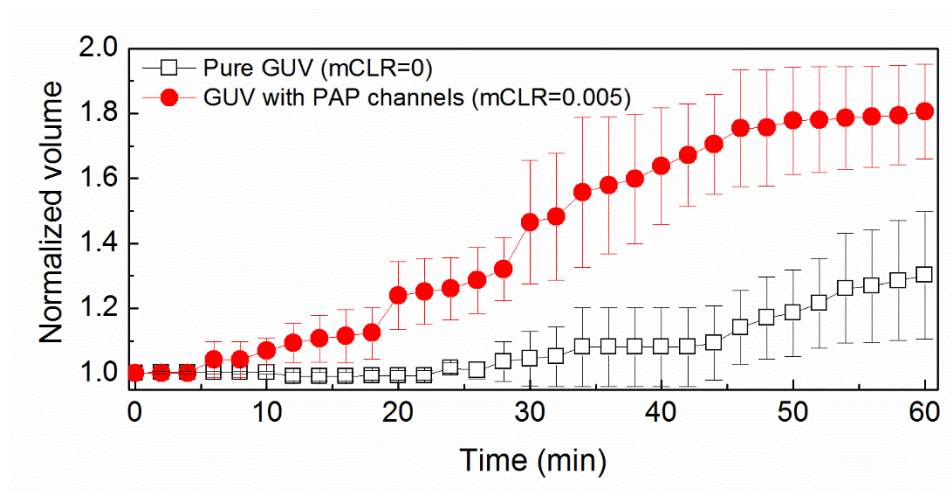


Fig. S2. Volume change of pure GUVs (mCLR=0) and GUVs with PAP channels (mCLR=0.005) after exposure to hypotonic solutions containing 20 mM less glucose. Data shown are the average of triplicates with error bars representing standard deviation.

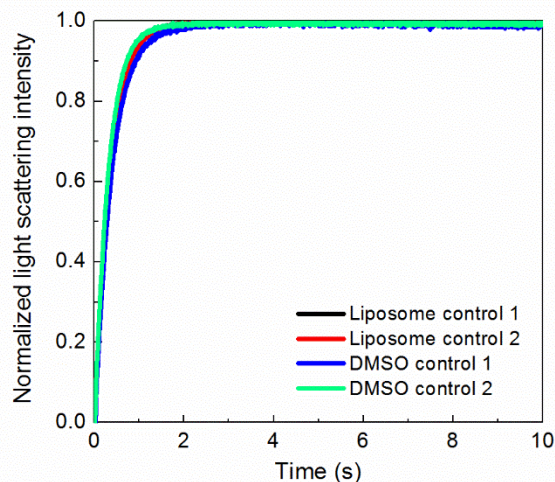


Fig. S3. Residual DMSO that may be present in processed liposomes has no measurable effect on the water permeability of liposomes. Liposomes were formed with phosphatidylcholine (PC) and phosphatidylserine (PS) lipids at a molar ratio of 4:1 in pure chloroform using the film rehydration method. In the DMSO controls, 40 μl DMSO was added in the film-making process, the same amount that was added when liposomes were formed in the presence of PAP channels. All samples were exposed to an abrupt increase in osmolarity by increasing the NaCl concentration of the buffer by 200 mM. Stopped-flow data showed no difference between samples with and without DMSO, indicating that the residual DMSO that may be present has no effect on the measured water permeability of the liposomes. The averaged permeability calculated from exponential constant k_2 of the samples including DMSO was 1.3×10^{-4} $\mu\text{m/s}$, which was close to the value of the samples without DMSO (5.4×10^{-4} $\mu\text{m/s}$). These numbers are orders of magnitude lower than the water permeability of vesicles with incorporated PAP channels.

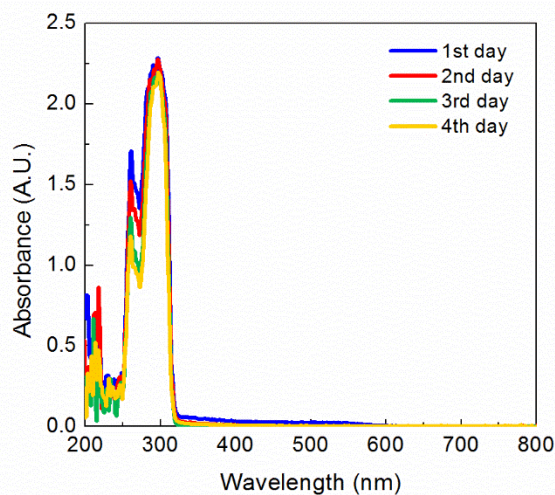


Fig. S4. The channels were almost completely retained during dialysis (~95%, based on Beer-Lambert law on the absorbance at 296 nm). UV-Vis spectra of PAP channel were recorded daily during dialysis against DMSO using a membrane with a 2-kDa cut-off. 100 μ L channel stock (5 mg/mL in DMSO) was injected into the dialysis tube. The dialysis solution was 300 mL DMSO, which was replaced with fresh DMSO every 12 h.

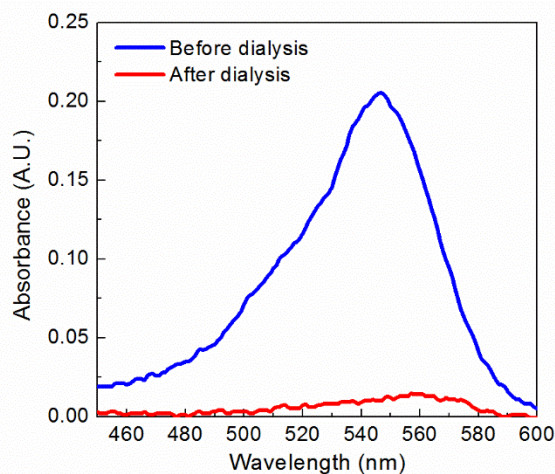


Fig. S5. Dye removal efficiency. The UV-Vis spectra of the dye were recorded before and after 3 days of dialysis against DMSO using a dialysis membrane with a 2-kDa cut-off. 10 μ L dye stock (50 mg/mL in DMSO) was diluted to 110 μ L and injected into the dialysis tube. The stripping DMSO was 300 mL and replaced with fresh DMSO every 12 h.

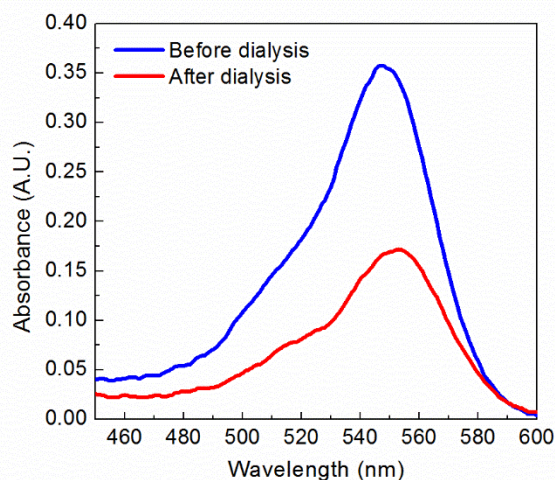


Fig. S6. Efficiency of labeling the channel with 5-(and-6)-((N-(5-aminopentyl)amino)carbonyl)tetramethylrhodamine. 100 μ L PAP channel (5 mg/mL in DMSO) was mixed with 9.18 μ L dye (50 mg/mL in DMSO) and 3.68 μ L DDC (50 mg/mL in DMSO) (stoichiometry of 1:10:10). The reaction was performed in the dark at room temperature on a stirring plate overnight. The solution was then injected into a dialysis tube and dialyzed against 300 mL DMSO using a 2-kDa cut-off membrane. The DMSO was replaced every 12 h. UV-Vis spectra of the labeled channel were recorded before and after 3 days of dialysis.

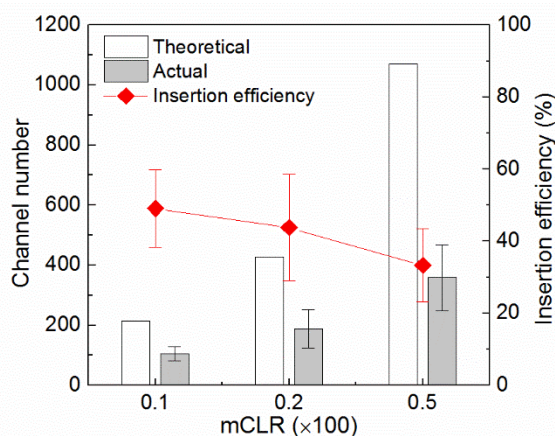


Fig. S7. The efficiency with which PAP channels were inserted into PC/PS liposomes. The theoretical insertion number was calculated in the following way: With a vesicle diameter of ~ 80 nm and assuming a bilayer thickness of 5 nm, the sum of outer and inner surface areas is $\pi/4 \times d^2 + \pi/4 \times (d-5)^2 = 151,110$ nm². The average cross-sectional areas of the lipid and PAP channel are 0.35 nm² and 3.0 nm², respectively. With an mCLR of 0.001, for example, the theoretical insertion number of the channel is 216 per vesicle. A similar method was used in Erbakan et al. (6) to determine the theoretical number of AQP channels per vesicle assuming 100% insertion efficiency. Data shown are the average of triplicates with standard deviation.

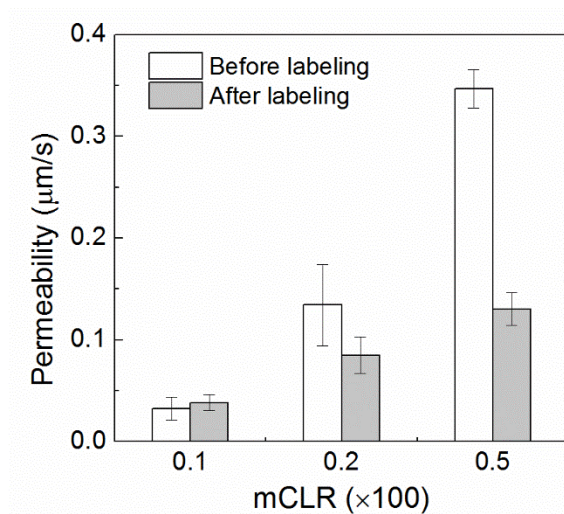


Fig. S8. Water permeability of the PAP channel before and after labeling with fluorescent dye. Stopped-flow experiments were performed on vesicles formed with different mCLRs. Labeling reduced the water permeability, especially for vesicles formed with an mCLR of 0.005 (data shown are average of triplicates with standard deviation). Lipids used for vesicle formation were a 4:1 (mol:mol) mixture of phosphatidylcholine and phosphatidylserine. Vesicles experienced an abrupt increase in osmolarity by exposing them to a buffer containing 400 mM sucrose. The data were fit to a double-exponential equation to calculate the exponential coefficient (k) for the initial change in the light scattering curve. The coefficient with the smaller value (k_2) increased with increasing mCLRs, indicating an increase in the permeability of the vesicles. The osmotic water permeability (P_f) was calculated according to: $P_f = k / ((S/V_0) \times V_w \times \Delta_{osm})$, where S is the initial surface area of the vesicles, V_0 is the initial volume of the vesicles, V_w is the molar volume of water, and Δ_{osm} is the osmolarity difference that drives transmembrane water flow and shrinking of the vesicles.

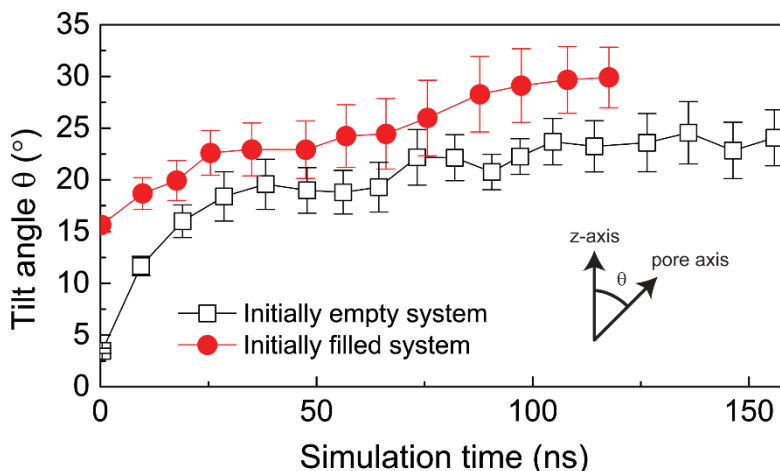


Fig. S9. Average tilt of PAP channels from the z axis for the simulations initiated with empty and water-filled channels. The channel axis was defined using the “measure inertia” command in VMD, which returned the normal vector of the plane defined by the positions of all non-hydrogen atoms of the inner ring of the channel. The tilt angle θ was defined as the angle between the z axis and the normal vector of the membrane plane, and it was calculated over the trajectory length for each channel after removal of restraints. For both systems, initiated with water-filled and empty channels, the data for each channel were subjected to a 10-ns block average, then averaged across all 25 channels in the system; each data point in the graph represents the mean tilt angle from the z axis of the 25 channels for a 10 ns interval, plotted with the standard error of the mean. The average tilt angle of the PAP channels converged for both systems within the simulated time.

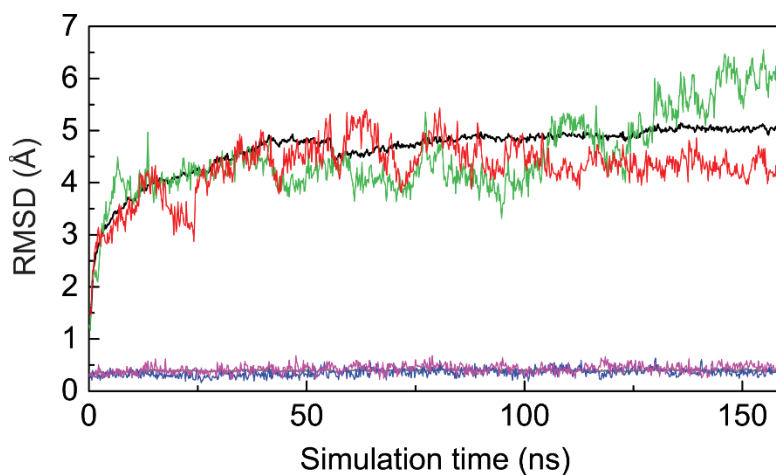


Fig. S10. The root mean square deviation (RMSD) of the coordinates of the PAP channels with respect to their crystallographic coordinates. The red and green traces represent the RMSD of the channel backbone of two representative channels, while the blue and purple traces represent the RMSD of the carbons in the central ring of the same two channels. The black trace represents the average RMSD of the channel backbone, which was calculated by summing up the RMSD trajectories for all channels in the simulation as vectors of length N and scaling the resulting vector by $1/M$, where N is the number of discrete points in each RMSD *versus* time trajectory and M is the number of channels.

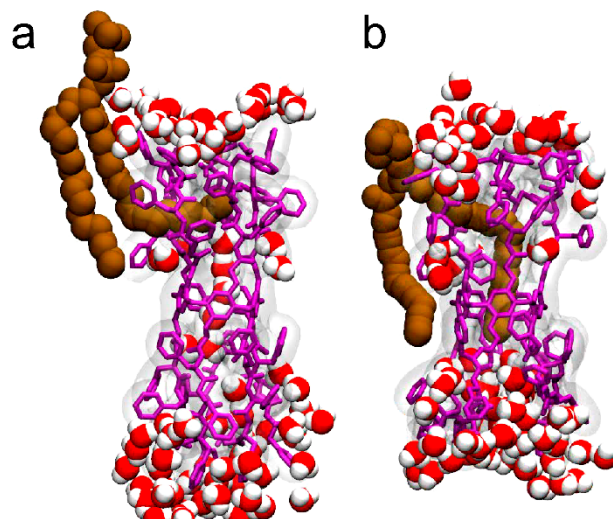


Fig. S11. PAP channel (purple licorice surrounded by translucent grey surface) pictured (a) before and (b) after infiltration by POPC lipid tail (ochre spheres). The oxygen and hydrogen atoms of water are shown in red and white, respectively. Panel a represents a single channel from the system with waters initially inserted, at the start of unrestrained simulation, while panel b represents the same channel 9 ns later.

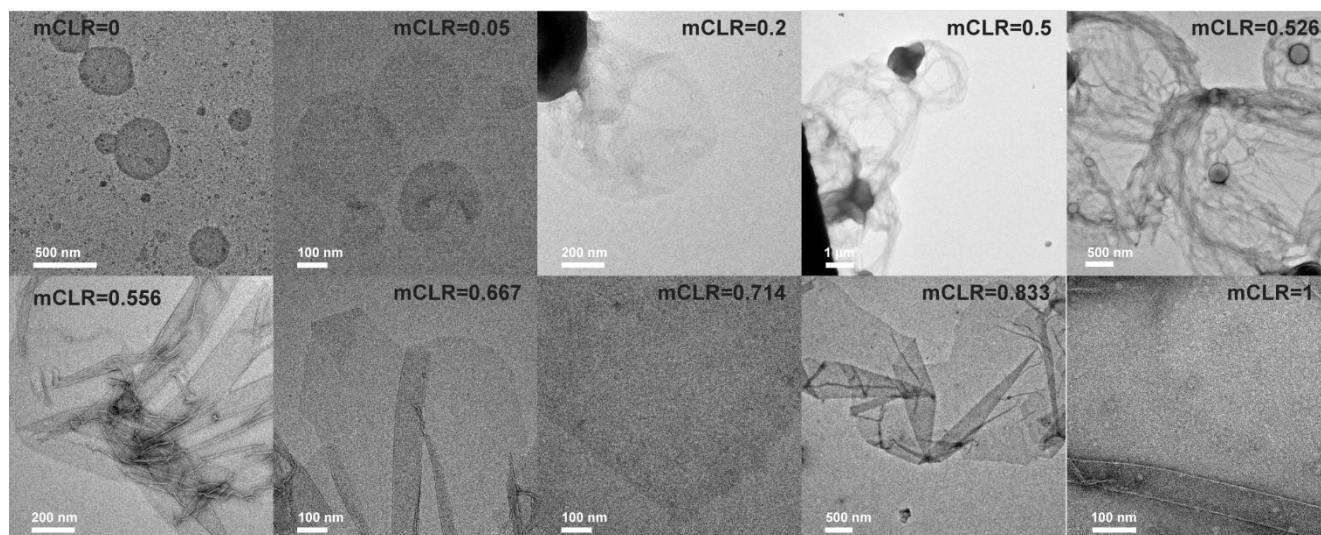


Fig. S12. Negative-stain EM images of PAP channel/lipid aggregates formed at different molar channel-to-lipid ratios (mCLRs). The dominant morphology of channel/lipid aggregates changes as a function of PAP channel density in the membranes from small vesicles to larger vesicles and finally flat membrane sheets.

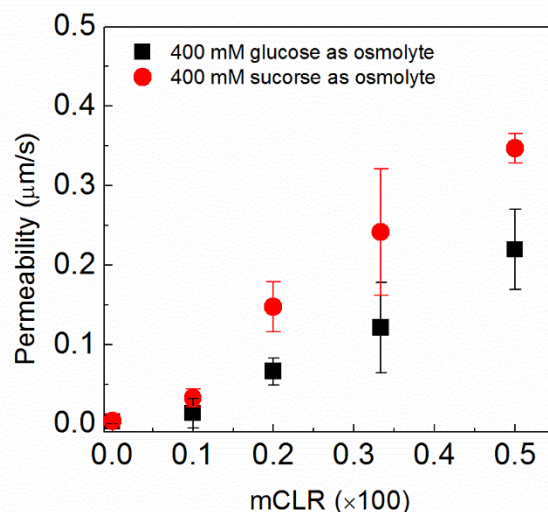


Fig. S13. The water permeability of vesicles containing PAP channels increases at different rates when glucose or sucrose is used as osmolyte (data shown are average and standard deviation of triplicate experiments). Vesicles were formed with a 4:1 (mol/mol) mixture of phosphatidylcholine and phosphatidylserine and using different mCLRs. Vesicles experienced an abrupt increase in osmolarity by exposing them to buffer containing 400 mM glucose or sucrose. The data were fit to a double-exponential equation to calculate the exponential coefficient (k) for the initial change in the light-scattering curve. The coefficient with the smaller value (k_2) increased with increasing mCLRs, indicating an increase in the permeability of the vesicles. The osmotic water permeability (P_f) was calculated by using the following expression: $P_f = k / ((S/V_0) \times V_w \times \Delta_{osm})$, where S is the initial surface area of the vesicles, V_0 is the initial volume of the vesicles, V_w is the molar volume of water, and Δ_{osm} is the osmolarity difference used to drive transmembrane water flux and thus shrinking of the vesicles.

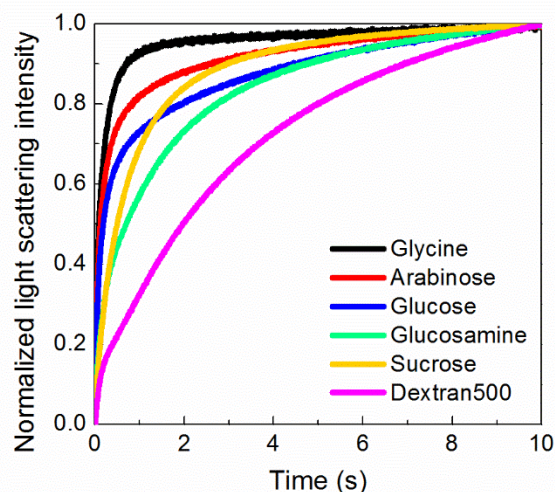


Fig. S14. Water permeability of vesicles containing PAP channels was measured using osmolytes of different molecular weights to determine the approximate pore size of the channel (stopped-flow data shown are representative single traces). The osmolytes used for the stopped-flow experiments were 400 mM glycine, 400 mM arabinose, 400 mM glucose, 400 mM glucosamine, 400 mM sucrose, and 200 mM Dextran500. The data were fit to a double-exponential equation. The second exponential coefficient (k_2) increased with increasing molecular size of the solute.

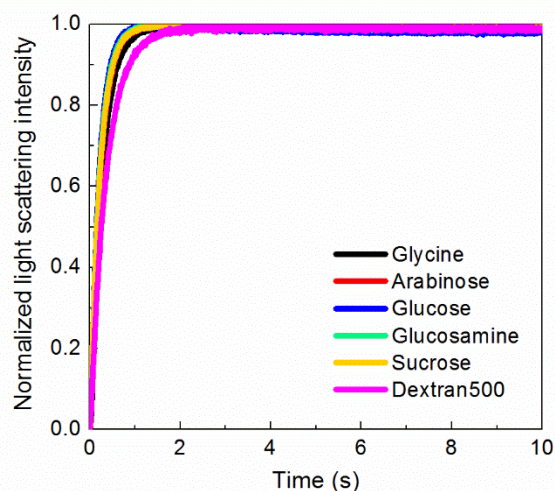


Fig. S15. Water permeability of pure lipid vesicles when measured in the presence of osmolytes of different molecular weights (stopped-flow data shown are representative single traces). The osmolytes used for the stopped-flow experiments were 400 mM glycine, 400 mM arabinose, 400 mM glucose, 400 mM glucosamine, 400 mM sucrose, and 200 mM Dextran500. The data were fit to a double-exponential equation. The second exponential coefficient (k_2) did not change with increasing molecular size of the solute.

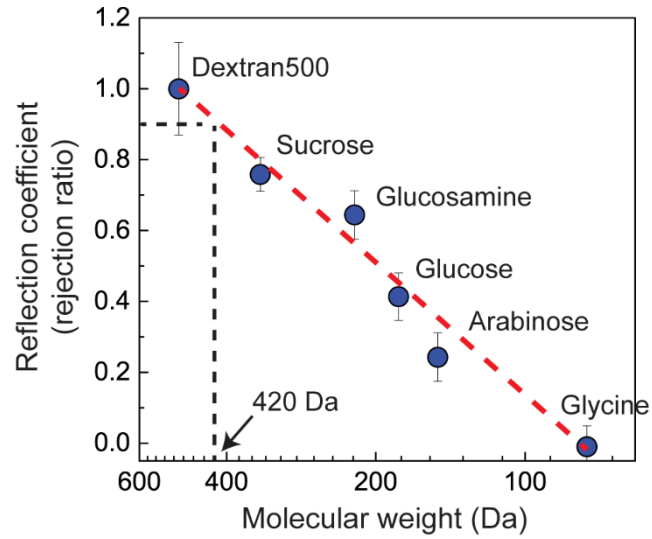


Fig. S16. The molecular weight cut-off of the PAP channel. Reflection coefficients (or rejection ratios, based on Dextran500) of the PAP channel were determined by stopped-flow light scattering measurements using osmolytes with different molecular weights. The actual osmolarity of each osmolyte was determined using a freezing point osmometer. The molecular weight cut-off based on a reflection coefficient of 0.9 was determined to be 420 kDa. Data shown are averages and standard deviations of triplicate experiments.

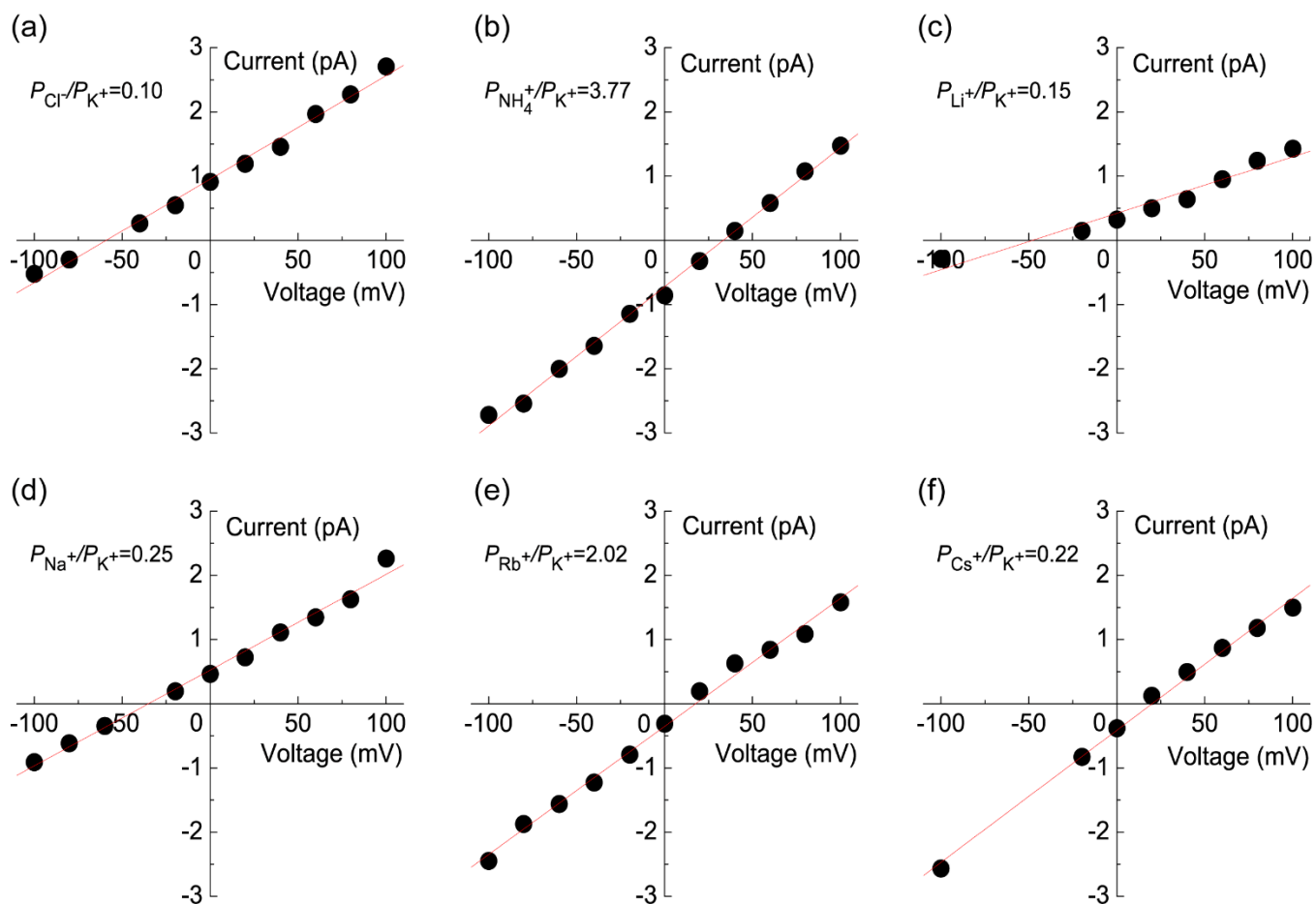


Fig. S17. The voltage-current relationship of the PAP channel obtained from patch-clamp experiments. The reversal potential, obtained from the measured voltage-current data, was used to calculate the ion selectivity based on the Goldman-Hodgkin-Katz equation. The order of ion selectivity was $NH_4^+ > Cs^+ > Rb^+ > K^+ > Na^+ > Li^+ > Cl^-$.

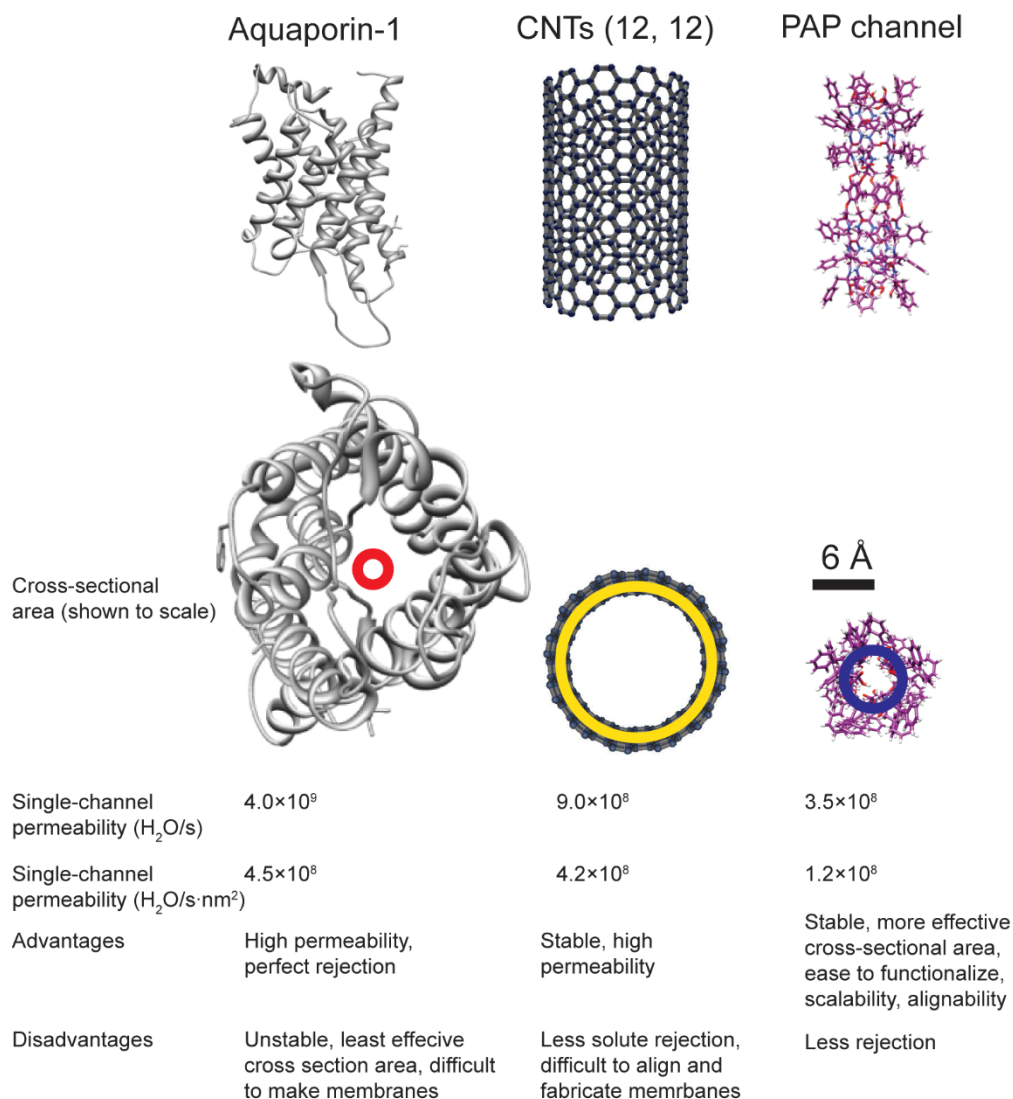


Fig. S18. Comparison of aquaporin-1, carbon nanotubes (CNTs, (12,12)) and the peptide-appended pillar[5]arene (PAP) channels. Inside circles indicate the actual pore size of these channels. The permeability and size of aquaporin-1 are from Zeidel *et al.* (36) and Murata *et al.* (37). The permeability data of CNTs are from Holt *et al.* (35) and Noy *et al.* (38). Holt *et al.* (35) estimated that the average diameter of the pore in their CNTs was 1.6 nm, close to the overall diameter of CNTs (12, 12). The permeability of the PAP channel was obtained from swelling experiments (Fig. 2C) and its cross-section area of $\sim 3.0 \text{ nm}^2$.